Mutations in *LNPK*, Encoding the Endoplasmic Reticulum Junction Stabilizer Lunapark, Cause a Recessive Neurodevelopmental Syndrome

Martin W. Breuss,[1,2] An Nguyen,[1,2] Qiong Song,[1,2] Thai Nguyen,[1,2] Valentina Stanley,[1,2] Kiely N. James,[1,2] Damir Musaev,[1,2] Guoliang Chai,[1,2] Sara A. Wirth,[1,2] Paula Anzenberg,[1,2] Renee D. George,[1,2] Anide Johansen,[1,2] Shaila Ali,[3] Muhammad Zia-ur-Rehman,[3] Tipu Sultan,[3] Maha S. Zaki,[4] and Joseph G. Gleeson[1,2,*]

The dynamic shape of the endoplasmic reticulum (ER) is a reflection of its wide variety of critical cell biological functions. Consequently, perturbation of ER-shaping proteins can cause a range of human phenotypes. Here, we describe three affected children (from two consanguineous families) who carry homozygous loss-of-function mutations in *LNPK* (previously known as *KIAA1715*); this gene encodes lunapark, which is proposed to serve as a curvature-stabilizing protein within tubular three-way junctions of the ER. All individuals presented with severe psychomotor delay, intellectual disability, hypotonia, epilepsy, and corpus callosum hypoplasia, and two of three showed mild cerebellar hypoplasia and atrophy. Consistent with a proposed role in neurodevelopmental disease, *LNPK* was expressed during brain development in humans and mice and was present in neurite-like processes in differentiating human neural progenitor cells. Affected cells showed the absence of full-length lunapark, aberrant ER structures, and increased luminal mass density. Together, our results implicate the ER junction stabilizer lunapark in establishing the corpus callosum.

The endoplasmic reticulum (ER) has numerous cellular functions that require distinct properties and shapes.[1,2] Therefore, the dynamic transition between and maintenance of distinct states are a tightly regulated process that involves a number of effectors and regulators.[3] Mutations in genes that encode these proteins have been implicated in a range of human disorders, including Alzheimer disease and hereditary spastic paraplegia (HSP), the latter of which has been studied extensively in connection with ER-shaping proteins.[4,5] For instance, heterozygous mutations in *ATL1* (MIM: 606439), encoding Atlastin-1, cause autosomal-dominant spastic paraplegia 3A (SPG3A [MIM: 182600]) and are the second most common cause of HSP.[4–6] SPG12 (MIM: 604805), SPG31 (MIM: 610250), and SPG72 (MIM: 515626) are likewise associated with mutations in *REEP1* (MIM: 609139), *RTN2* (MIM: 603183), and *REEP2* (MIM: 609347), respectively.[7–9] These and other mutations have provided a strong link between ER-shaping proteins and the health of neurons that have extended axonal projections, such as the corticospinal motor neurons that exhibit the hallmark axonopathy in HSP.[5]

The transmembrane protein lunapark (encoded by *LNPK*, also known as *KIAA1715* [MIM: 610236]) is a more recent addition to the extended list of proteins that are involved in regulating ER shape.[10] *Lnpk*, the mouse homolog of this gene, was originally described as part of the *HoxD* cluster that is critical for digit development and was named after the conserved L-N-P-A-R-K peptide motif found in its protein product.[11,12] The protein consists of an N-terminal domain important in N-myristoylation and ER targeting, two transmembrane domains, and a unique zinc-finger domain with a proposed role in oligomerization.[13,14] Current evidence and models suggest that lunapark mainly acts as a stabilizer of negative membrane curvature and thereby maintains three-way junctions of tubular ER through its localization to these structures.[13,15,16] Although its cellular role has been described, its functional importance in mammals is currently unclear. The sole organismal phenotype to date was described in *C. elegans* and comprises locomotor defects and mislocalization of presynaptic proteins.[17]

We identified two consanguineous families that carry loss-of-function (LoF) *LNPK* mutations that are associated with severe neurodevelopmental disease. Family A included two affected children (A-III-1 and A-III-2), both diagnosed with global developmental delay and seizures, from a first-cousin marriage (Figure 1A, Table 1, and Table S1). There were no reported prenatal or birth complications, and weight, length, and head circumference were unremarkable. At the last examination (15 and 7 years of age for A-III-1 and A-III-2, respectively), both individuals exhibited psychomotor developmental delay, intellectual disability, defects in social interactions, hyperactivity, and inattention. The older child was more severely affected and showed signs of regression and affected motor functions, including hypotonia, rigidity, and an inability to speak or walk, whereas the younger sibling suffered from only mild hypotonia and abnormal gait (Table 1 and Table S1). Both exhibited mainly myoclonic seizures as early as 2 years of age. Whereas the younger sibling's epilepsy

[1]Department of Neurosciences, Howard Hughes Medical Institute, University of California, San Diego, La Jolla, CA 92093, USA; [2]Rady Children's Institute for Genomic Medicine, San Diego, CA 92025, USA; [3]Department of Pediatric Neurology, Children's Hospital and Institute of Child Health, Lahore 54000, Pakistan; [4]Clinical Genetics Department, Human Genetics and Genome Research Division, National Research Centre, Cairo 12311, Egypt
*Correspondence: jogleeson@ucsd.edu
https://doi.org/10.1016/j.ajhg.2018.06.011.

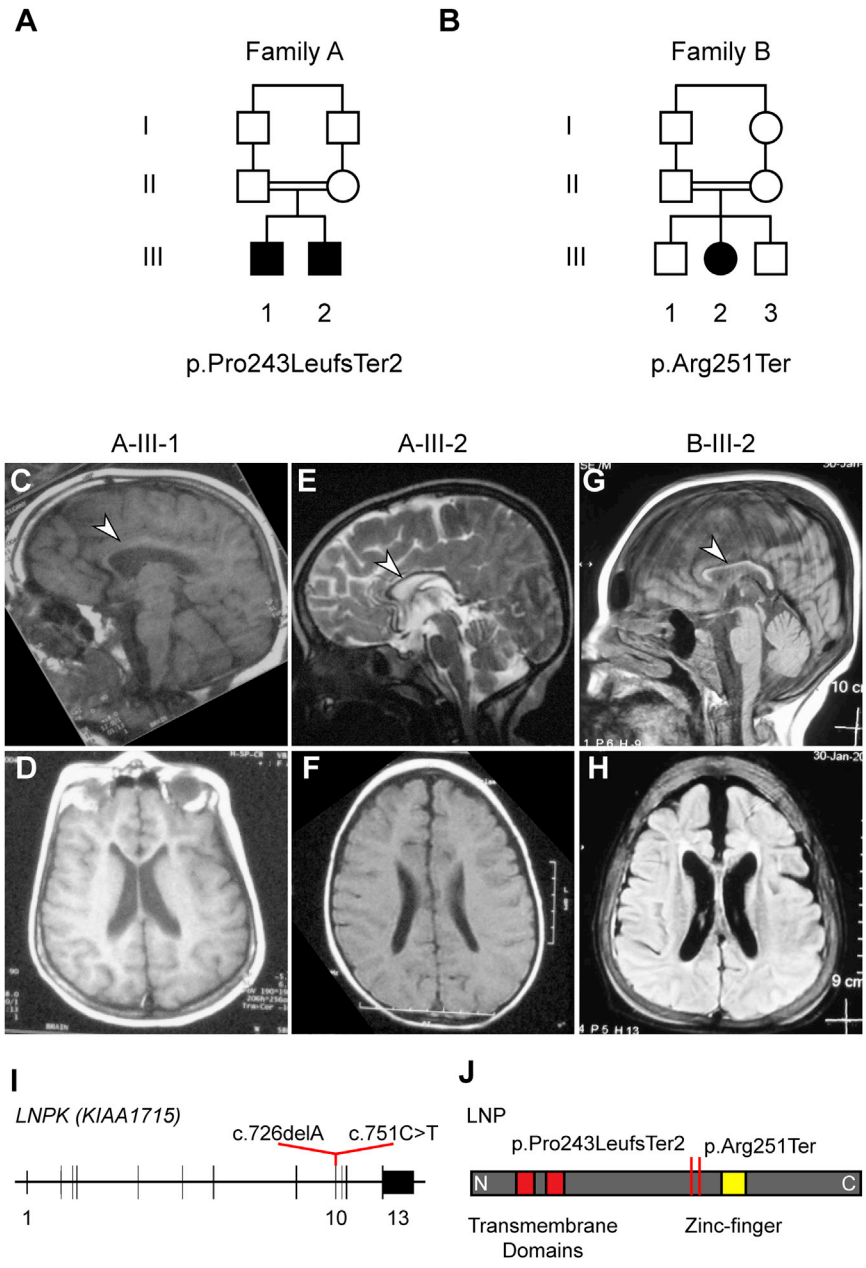

Figure 1. Clinical and Genetic Information for families A and B

(A and B) Family pedigrees for families A and B. Affected children in both families are from consanguineous parents (double line indicates first cousins).

(C–H) T1-weighted (D and F–H), T2-weighted (E), and FLAIR (C) MRI for individuals A-III-1 (C and D), A-III-2 (E and F), and B-III-2 (G and H). Shown are sagittal (C, E, and G) and axial (D, F, and H) images. Arrowheads indicate the corpus callosum hypoplasia common to all three affected children. Other brain regions appear largely unaffected with the exception of mild cerebellar affectation in A-III-2 and B-III-2.

(I) Schematic of *LNPK* depicts the genomic sequence spanning 13 exons. Red lines indicate the position of the two mutations in exon 10 and show their coordinates within the cDNA (GenBank: NM_030650.2).

(J) Schematic of the lunapark protein (LNP) depicts the location of the two transmembrane domains (red) and the zinc finger (yellow). N and C indicate the N and C termini of the protein, respectively. Red lines indicate the position of the two truncating mutations upstream of the zinc finger and the effect of the two mutations on the protein level (GenBank: NP_085153.1).

was controlled with anticonvulsants, the older sibling's seizures were refractory (Table 1 and Table S1). Brain MRI of both children revealed no involvement of the cortical structures but did show corpus callosum hypoplasia in both and mild cerebellar vermis hypoplasia in the younger child (Figures 1C–1F).

Family B had one affected girl (B-III-2) and two healthy siblings from a first-cousin marriage (Figure 1B). There were no reported prenatal or birth complications, and weight, length, and head circumference were unremarkable. The girl's last examination (at 13.5 years of age) revealed a significantly more severe clinical course than what was observed in family A: she was bedridden in a vegetative state and showed severe tremor and dysmetria with purposeful movement (Table 1 and Table S1). Her phenotype was slowly progressive, and she experienced frequent infections. She had generalized tonic-clonic epileptic seizures starting at 1 year of age, and her brain MRI showed corpus callosum hypoplasia and mild cerebellar atrophy; no abnormalities were seen in other brain areas (Figures 1G and 1H).

After informed consent was acquired from all participating individuals in accordance with the ethical standards of the responsible committee on human experimentation at the University of California, San Diego, whole-exome sequencing (WES) was performed on blood-derived DNA from both affected children from family A and the mother, father, and affected girl from family B. Blood-derived DNA from both parents in family A and both unaffected siblings in family B was used for segregation testing. For variant identification and prioritization, we employed our internal pipeline, which implemented minor allele frequency (public and internal), as well as PolyPhen-2 prediction and GERP scores as previously described (see also Supplemental Material and Methods).[18,19] Only one remaining candidate in family A segregated with the phenotype: a frameshift-causing deletion in exon 10 of *LNPK* (c.726delA [p.Pro243LeufsTer2] [GenBank: NM_030650.2]) (Figures 1I and 1J). Likewise,

Table 1. Mutations in *LNPK* Cause Various Phenotypes, Including Corpus Callosum Hypoplasia, Hypotonia, and Epilepsy

	Individual		
	A-III-1	**A-III-2**	**B-III-2**
Genomic mutation	chr2: 176804365GT>G (hg19[a])	chr2: 176804365GT>G (hg19[a])	chr2: 176804341G>A (hg19[a])
cDNA mutation	c.726delA	c.726delA	c.751C>T
Protein variant	p.Pro243LeufsTer2	p.Pro243LeufsTer2	p.Arg251Ter
Gender	male	male	female
Origin	Egypt	Egypt	Pakistan
Consanguinity	first cousin	first cousin	first cousin
Age at diagnosis	15 years	7 years, 4 months	14 months
Psychomotor Development			
Gross motor skills	delayed	delayed	significantly delayed
Fine motor skills	delayed	delayed	significantly delayed
Language skills	absent	delayed	significantly delayed
Social skills	delayed	delayed	significantly delayed
Regression	progressive	stationary	progressive (bedridden)
Neurological Findings			
Higher cognitive functions	severe intellectual disability, no speech, autistic features, very limited social interaction, hyperactivity, inattention, dementia	intellectual disability, a few unclear words, mild autistic features, hyperactive, inattention, minimal aggressiveness	vegetative state
Extrapyramidal symptoms	rigidity, drooling	no data	rigidity
Cerebellar deficits	no	no	bedridden
Motor deficits	hypertonia, only crawling	ambulatory	flaccid
Muscle tone	hypotonia with rigidity	mild hypotonia	flaccid
Reflexes	present	present	flaccid
Sensory	normal	normal	not possible
Gait	incapable	wide based	ataxia
Seizures			
Age of onset	2 years	2 years	1 year
Type(s)	myoclonic, tonic, and extension spasms	myoclonic	generalized tonic clonic
Most frequent type	myoclonic	myoclonic	generalized tonic clonic
Frequency	every several days	controlled	unknown
Treatment	valproate, levetiracetum, clonazepam	valproate, levetiracetum	valporate, carbamazepine
MRI Findings			
Corpus callosum	hypoplasia	hypoplasia	hypoplasia
Cerebellum	normal	mild vermian hypoplasia	atrophy

[a]UCSC Genome Browser hg19.

in family B, we identified only one high-impact variant that was located in *LNPK* (c.751C>T [GenBank: NM_030650.2]) and resulted in a LoF allele (p.Arg251Ter) (Figures 1I and 1J). Thus, the similar location of the LoF variants, as well as the matching phenotypes, rendered the *LNPK* mutation a likely disease-causing candidate.

Neither of the *LNPK* variants was reported in our unrelated cohort of over 5,000 individuals (the GME Variome) or in the Exome Aggregation Consortium (ExAC) Browser or gnomAD.[19,20] Consistent with the fact that this gene is sensitive to LoF mutations, no other homozygous LoF mutations have been reported in the ExAC Browser; likewise, its pNull score, a metric that reflects the likelihood that a given gene is neutral to both heterozygous and homozygous loss, is 0.00.[20] Both variants are adjacent to or within a stretch of extended homozygosity

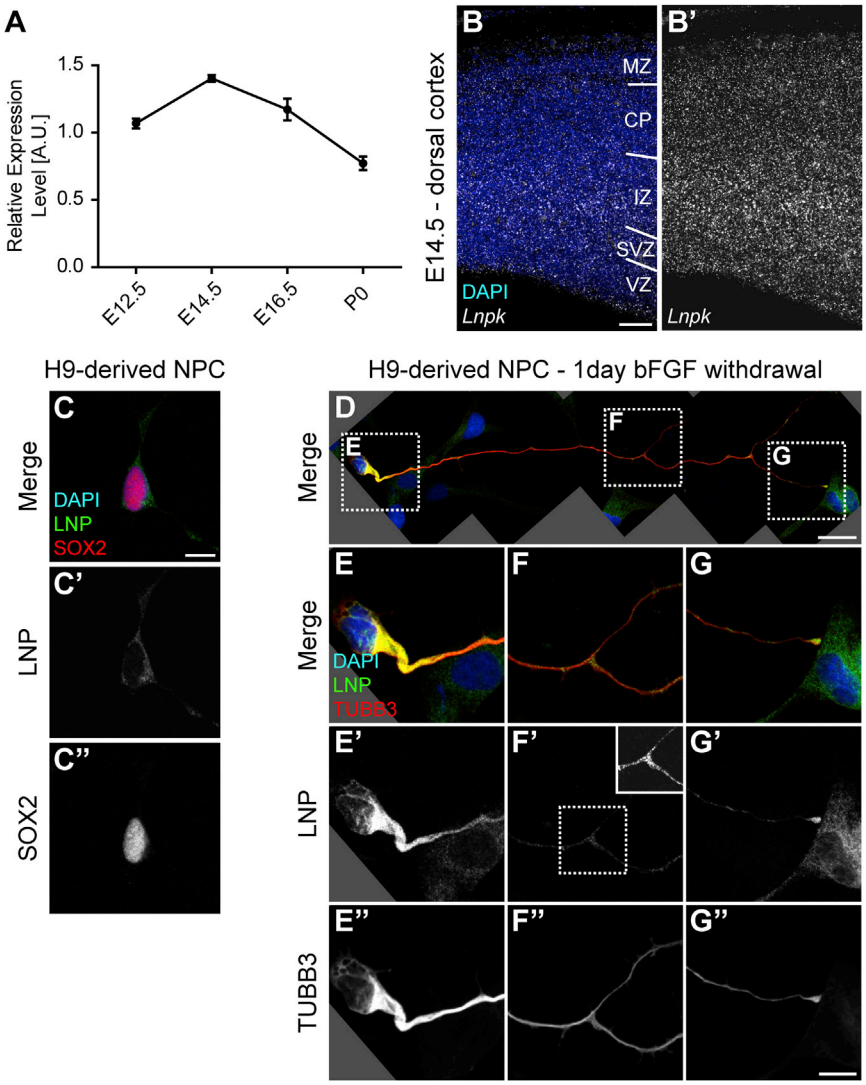

Figure 2. Localization of Lunapark in Mice and Humans

(A) Graph showing the expression of mouse *Lnpk* in relation to the geometric mean of three housekeeping genes via quantitative RT-PCR. Time points range from embryonic day 12.5 (E12.5) to postnatal day 0 (P0). Graph shows mean ± SEM for each time point. n = 3 animals.

(B) Image of *in situ* hybridization using RNAscope against the *Lnpk* mRNA transcript. Shown are DAPI and the *in situ* signal. B′ shows the *Lnpk* signal alone for better visualization. Abbreviations are as follows: VZ, ventricular zone; SVZ, subventricular zone; IZ, intermediate zone; CP, cortical plate; and MZ, marginal zone.

(C) Image shows an H9-derived NPC stained with DAPI and antibodies against LNP and SOX2. C′ and C″ show gray-scale images of the indicated channels.

(D–G) Images show an H9-derived NPC, driven toward differentiation by 1 day of bFGF withdrawal, stained with DAPI and antibodies against LNP and TUBB3 (Tuj). Shown are an overview (D), magnification of the soma (E), magnification of a process branch point (F), and magnification of the tip of the extending process (G). In addition to the merged image (E–G), gray-scale images of the LNP and TUBB3 channels are shown (E′–G′ and E″–G″, respectively). LNP appeared to be upregulated in differentiating NPCs and also accumulated in branch points and the tip of the extending neurite that was reminiscent of an axonal growth cone. The inlay in (F′) shows the boxed area with higher contrast for better visualization of the increased signal of LNP at the branching point. Scale bars represent 50 μm (B), 10 μm (C and G″), and 25 μm (D).

(HomozygosityMapper; Figure S1) and are also predicted to cause LoF by MutationTaster.[21,22] The mutations in families A and B fall within the same exon and introduce premature stop codons that should both result in truncations of the protein product before the two zinc fingers (Figures 1I–1J and Figure S2).

LNPK was found to be ubiquitously expressed in adult human tissues (Genotype-Tissue Expression [GTEx] data) and in human (BrainSpan data) and murine brain development at all assessed stages (Figure 2A and Figures S3 and S4). Spatially, at embryonic day 14.5 (E14.5), its expression was detected across all areas of the developing murine brain by *in situ* hybridization (Figure 2B and Figure S5). Both dorsal and ventral cortices showed similar localization of the transcript across the entire area, suggesting that *Lnpk* is expressed in both progenitor cells and postmitotic neurons in mice.

The human lunapark protein (LNP) was likewise present in human neural precursor cells (NPCs) derived from embryonic stem cells (Figure 2C). In a differentiated state, driven by the withdrawal of FGF for 1 day, NPCs exhibited an overall increase in LNP intensity (Figure 2D). In addition, neurite-like processes extended by the differentiating cells accumulated LNP at branching sites and at the growth-cone-like structure at the tip (Figures 2D–2G). This is consistent with the occurrence of tubular ER at the equivalent neuronal structures.[23] Together, the spatiotemporal expression patterns of human *LNPK* and its mouse ortholog are consistent with a role in neurodevelopment and support the pathogenicity of LoF mutations in this gene.

We obtained fibroblasts after acquiring informed consent from the affected girl and the mother in family B to test the impact of the premature stop variant (p.Arg251Ter). mRNA transcript levels, as assessed by quantitative RT-PCR, showed a notable reduction of the cells derived from the affected girl (B-III-2-(A)) (Figure 3A). Moreover, relative to the control fibroblasts, the maternal cells (B-II-2(M)) likewise exhibited reduced transcript levels of around 50%. Consequently, there was also no evidence of the full-length protein in whole-cell lysates from cells derived from the affected girl (Figures 3B and 3C). The

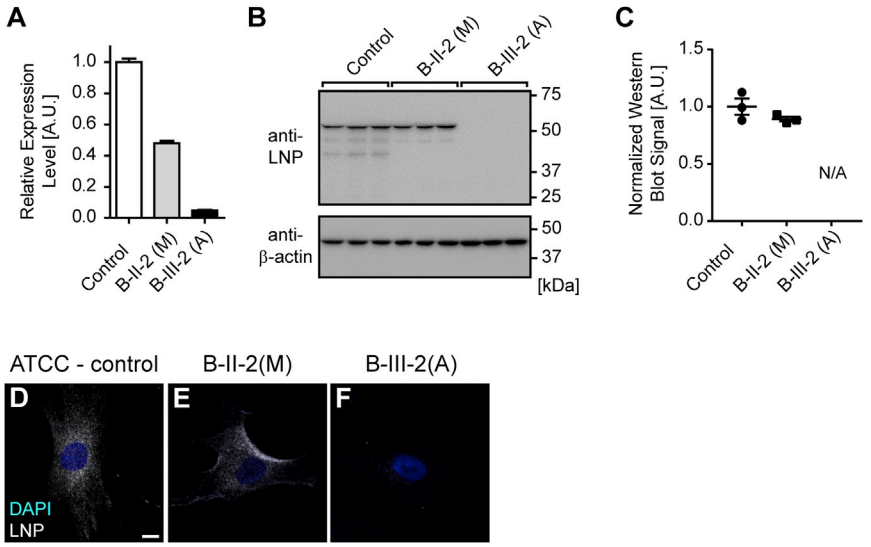

Figure 3. The Premature-Stop-Codon Mutation in *LNPK* Results in Loss of Transcript and Full-Length Protein

(A) Graph showing the expression of human *LNPK* in relation to the geometric mean of three housekeeping genes via quantitative RT-PCR. Compared are control fibroblasts (control) and fibroblasts derived from the unaffected mother (B-II-2(M)) and the affected girl (B-III-2(A)) from family B. Consistent with NMD due to a premature stop codon, *LNPK* levels are reduced by approximately 50% in B-II-2(M) and almost completely lost in B-III-2(A). n = 3 independent experiments.

(B) Western blot images probing for full-length LNP and β-actin in parallel blots with the same input. Shown are triplicates for the three conditions described before. Neither full-length nor truncated LNP signal could be detected for B-III-2(A).

(C) Quantification of blots shown in (B). LNP was normalized to β-actin. For B-III-2(A), no peaks could be identified for quantification. Note that the severe transcript reduction is not reflected at the protein level for B-II-2(M). Shown are individual data points, as well as the mean ± SEM.

(D–F) Images show representative examples of fibroblasts stained with DAPI and the antibody detecting LNP for all three conditions. Results confirm the absence of full-length protein in cells derived from the affected girl. The scale bar in (D) represents 10 μm.

protein also could not be detected by immunocytochemistry (Figures 3D–3F).

Although the depletion of mRNA transcript, presumably through nonsense-mediated decay (NMD), suggested a loss of protein product, we could not completely exclude the presence of mutant protein. Although the currently employed antibody demonstrated the loss of full-length protein, it was unable to detect the truncated protein products (data not shown). Thus, we wanted to assess whether the mutant proteins were stable if ectopically expressed. After transfection of expression vectors for wild-type LNP and both truncations, the two mutants showed a punctate pattern reminiscent of wild-type LNP (Figure S6). This was consistent with the retained integrity of the transmembrane domains and with previous work that demonstrated that localization to the ER depends on the N terminus of LNP.[14] The expressed constructs were more stable than the wild-type (Figures S6A and S6B), suggesting that any residual mRNA could be transcribed into a functional protein with decreased cellular turnover. Despite these findings, the lack of mRNA transcripts suggests that the main pathogenic mechanism of these truncation mutations is a loss of protein; yet, we cannot exclude a contribution of the truncated protein to the phenotype in any way given that both mutants appear to be stable if expressed.

The effects of lunapark perturbation have been previously demonstrated by RNAi knockdown and genetic knockout in cell lines.[13,15] Its loss resulted in a reduction of tubular ER structures and an increased sheet-like appearance at the cellular periphery. This phenotype was observed in various cell lines in which each cell has a large surface area, ideal for imaging ER defects. Fibroblasts are less suited for these analyses because they typically have a spindle-like shape and less peripheral, tubular ER than the cell lines typically employed for these analyses. Thus, standard light microscopy would not provide sufficient resolution for assessing ER phenotypes in these cells. Therefore, we used electron microscopic assessment of the ER of pelleted cells to detect any potential phenotypes caused by loss of *LNPK* (Figure 4). All three fibroblast lines—control, B-II-2(M), and B-III-(A)—showed some variability with regard to ER structure as a result of both cellular variability and the angle of sectioning for individual cells. Nevertheless, aberrant ER structures were much more frequently present in the affected child's cells (9/15) than in the maternal (3/14) or control (1/17) cells (Figures 4A–4F and Figure S7). The observed phenotype mainly consisted of a more sheet-like, less compact appearance, a reduced contrast of the membranous structure surrounding the ER, and decreased brightness of the lumen, indicative of higher mass density within the ER (Figure 4F).[24] This is similar to what has been described in a mouse model with increased ER stress.[25]

We confirmed the increased luminal mass density by blinded, unbiased stereology, where we assessed the average gray values at points that were classified as either ER or part of the remaining cellular area (Figure 4G).[26] When we compared the overall cellular brightness (non-ER) with the specific ER signal within each category, only the affected fibroblasts were significantly darker in the ER lumen (Figure 4G). Employing the same, unbiased stereology dataset, we found no detectable difference between the fractional abundance of ER and all assessed points within the cellular area (Figure 4H). Together, these data suggest that defects in ER shape and luminal composition in fibroblasts, but not defects in the overall ER size relative to the

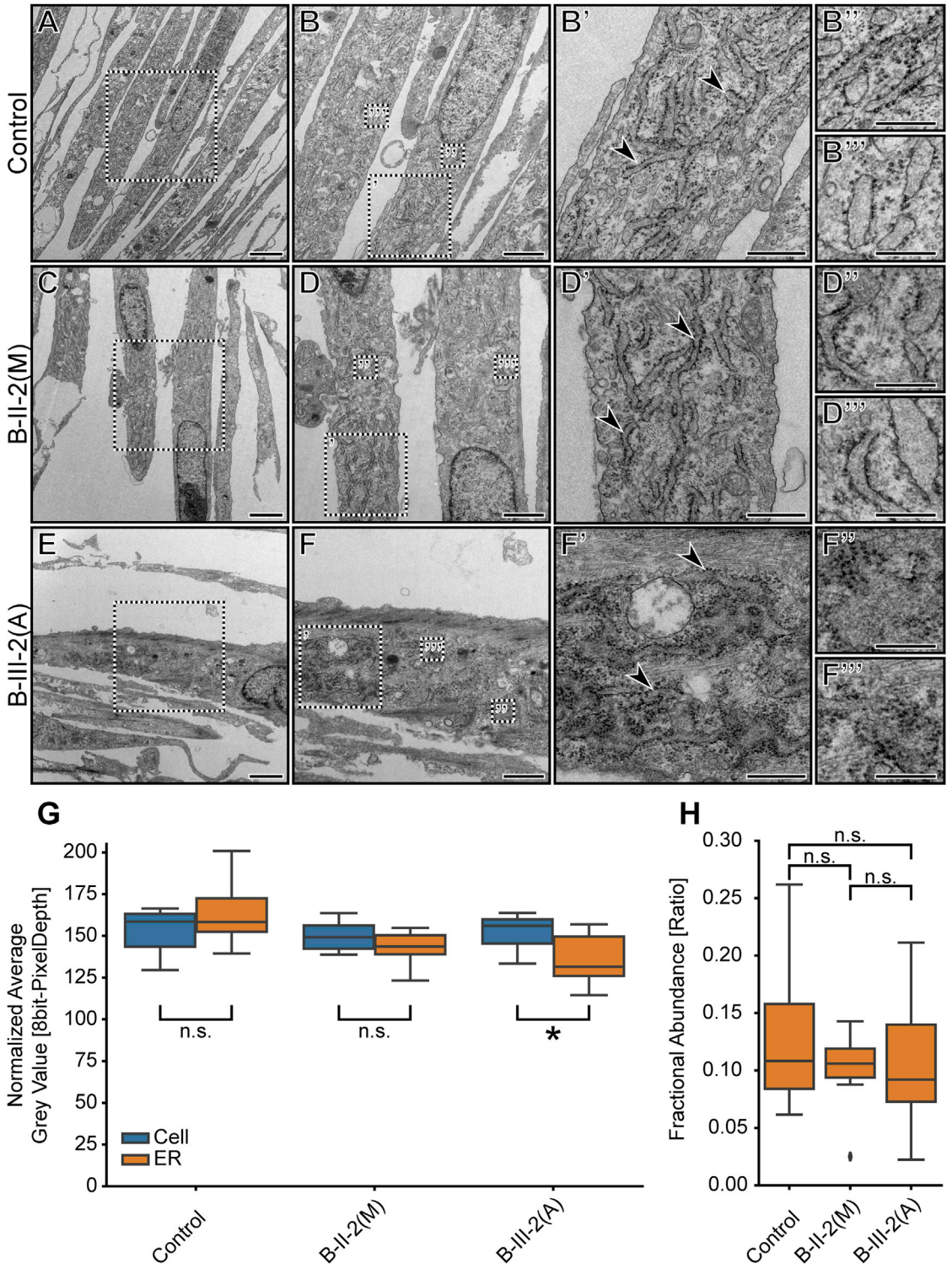

Figure 4. Fibroblasts Harboring a Homozygous, Truncating Mutation in *LNPK* Exhibit Aberrant ER Shape and Increased Luminal Mass Density

(A–F) Electron microscopy images of control fibroblasts (control) and fibroblasts derived from the unaffected mother (B-II-2(M)) and the affected girl (B-III-2(A)) from family B. Higher-magnification images (B, D, and F) also contain boxed regions that are shown on the right with the corresponding ′, ″, and ‴ labels. Arrowheads in (B′), (D′), and (F′) indicate rough ER that was used for the subsequent analysis and point out the disturbed ER morphology in (F′). Scale bars represent 2 μm (A, C, and E), 1 μm (B, D, and F), 500 nm (B′, D′, and F′), and 250 nm (B″, B‴, D″, D‴, F″, and F‴).

(G) Graph depicting the normalized average gray value of cellular positions that were classified as either cellular (excluding ER; cell) or rough ER (ER) for the three conditions introduced above. Points were selected by unbiased stereology (see Material and Methods). The average gray value was used as a proxy for luminal mass density. Statistical analysis for simple effects within rows (two-way ANOVA and

(legend continued on next page)

cellular size, are due to loss of *LNPK* (according to the fractional abundance measurement).

Here, we have described two unrelated, consanguineous families with three affected individuals who exhibited a similar phenotypic spectrum comprising hypotonia, movement disorders, epilepsy, and corpus callosum hypoplasia. In both families, the phenotype segregates with a LoF mutation in *LNPK*, encoding the protein lunapark.

The cellular role of lunapark was unknown until a recent study demonstrated its role in ER structure.[10] Before this, its function was explored only once, in the context of *C. elegans*, where its localization was dependent upon a kinesin microtubule motor, and its deletion resulted in motor defects and mislocalization of presynaptic proteins.[17] Although the authors were not able to link these phenotypes to a molecular function, the additional insights provided more recently permit connections from the phenotypes in *C. elegans* to the protein's localization to tubular ER junctions and its function in regulating ER shape.[13,15,16] Animals with the *lnp1* deletion exhibited subtle motor defects, reminiscent of the movement phenotypes in the three affected individuals.[17] Furthermore, a presynaptic vesicle defect, as described by the authors, might contribute to the observed epilepsy phenotype.

How does LoF of lunapark result in human phenotypes? Axonal ER fulfills many roles in developing and mature axons and requires extensive, active shaping and maintenance.[23] This is exemplified by the aforementioned defects in ER-shaping molecules that were implicated in spastic paraplegia almost two decades ago.[5,6] This finding suggested that neurons with extended axons are uniquely susceptible to perturbations of this organelle.[5] In addition to the maintenance of extended processes, the same regulation of the tubular structure of ER also appears to be critical for their formation: Zhu et al. demonstrated that the SPG3A protein Atlastin-1 was not only localized to active growth cones but also critical for axon extension.[27] Lunapark has been described by several lines of evidence to stabilize nascent three-way junctions of tubular ER.[13,15,16] Its localization to extending processes, as demonstrated in differentiating NPCs in this manuscript, is consistent with current knowledge of the localization of tubular ER structure in growing axons.[23]

More recent work has also suggested the involvement of lunapark in the formation of stacked membrane discs and the integrity of nuclear pore complexes.[28,29] It is unclear to what extent the multiple functions assigned to lunapark could contribute to the range of phenotypes found in the three affected children. Yet, given the similarities to disorders associated with other genes that encode ER-shaping proteins, we propose that this cellular function is responsible for the observed phenotypes. Although there are differences in clinical presentation, the phenotypes of the three affected children resembled those found for dominant-negative mutations in *ATL1* in SPG3A.[30] Although the hallmark spasticity is largely absent, limb weakness, delayed motor development, and variable impairment of mobility are shared. Structurally, Orlacchio et al. have described a case where a heterozygous *ATL1* variant resulted in a thin corpus callosum.[31] Moreover, epilepsy and intellectual disability have both been described in other forms of hereditary spastic paraplegia.[5]

Given the strong connection between ER-shaping molecules and human disease, it would be interesting to screen for hitherto unknown genes that are involved in this pathway and test their relevance in human disease. We and others have performed a similar approach for cilia genes to yield new insights into biology and disease.[32,33]

The function of lunapark at the organismal level has been poorly understood, and most functional insights derive from *in vitro* analysis of cell lines and unicellular yeast.[10,13–15] The identification of homozygous LoF mutations in individuals with corpus callosum hypoplasia suggests that its function, similar to that of Atlastin-1, is important for neurite extension, maintenance, or both. In future studies, it will be interesting to see what exact role lunapark has during the dynamic extension of growing axons and how this differs from or confirms the insights obtained from cell lines.

Accession Numbers

The accession number for the data reported in this article is dbGaP: phs000288.v1.p1.

Supplemental Data

Supplemental Data include Supplemental Material and Methods, seven figures, and two tables and can be found with this article online at https://doi.org/10.1016/j.ajhg.2018.06.011.

Acknowledgments

We are indebted to the families for their participation in this study. This work was supported by NIH grants R01NS048453 and R01NS052455, the Simons Foundation Autism Research Initiative 275275, and the Howard Hughes Medical Institute (to J.G.G.).

Sidak's multiple-comparison test) showed a significant difference between the ER gray values of the control and both B-II-2(M) ($p = 0.0018$) and B-III-2(A) ($p < 0.0001$) but not between the two lines from family B ($p = 0.5662$) or between any cellular gray values ($p > 0.95$ for all). Statistical analysis for effects within a column (two-way ANOVA and Sidak's multiple-comparison test) showed a significant difference between the cellular and ER gray values for B-III-2(A) (*$p = 0.0106$) but not for either the control (n.s., $p = 0.1930$) or B-II-2(M) (n.s., $p = 0.4789$). $n \geq 10$ EM images.

(H) Graph depicting the fractional abundance of ER positions in relation to the sum of all positions with a cell. Points were selected by unbiased stereology (see Material and Methods) and the same as used for (G). The fractional abundance was used as a proxy for volume (size) ER changes relative to the cell. No significant differences (n.s.) could be observed between any of the conditions (one-way ANOVA and Tukey's multiple-comparison test).

M.W.B. was supported by an EMBO Long-Term Fellowship (ALTF 174-2015), which is co-funded by the Marie Curie Actions of the European Commission (LTFCOFUND2013 and GA-2013-609409). The authors thank Susan Ferro-Novick and Peter Novick for reagents and their critical reading of the manuscript. We would also like to thank the following core services: the University of California, San Diego Neuroscience Core and Jennifer Santini for microscopy assistance (NIH grant NS047101), Dr. Marilyn Farquhar for the use of the electron microscopy facility, Ying Jones for electron microscopy sample preparation, and Timothy Meerloo for assistance with microscopy. The authors thank the Broad Institute (NIH grants U54HG003067 to E. Lander and UM1HG008900 to D. MacArthur), Yale University (NIH grant 5UM1HG006504-07), and Baylor College of Medicine (NIH grant 5UM1HG006542-07) for sequencing support and analysis. The Genotype-Tissue Expression (GTEx) Project was supported by the Common Fund of the NIH Office of the Director and by the National Cancer Institute, National Human Genome Research Institute, National Heart, Lung, and Blood Institute, National Institute on Drug Abuse, National Institute of Mental Health, and National Institute of Neurological Disorders and Stroke. The data used for the analyses described in this manuscript were obtained from the GTEx Portal on March 3, 2018.

Declaration of Interests

The authors declare no competing interests.

Received: May 7, 2018
Accepted: June 27, 2018
Published: July 19, 2018

Web Resources

BrainSpan: Atlas of the Developing Human Brain, http://www.brainspan.org/
dbGaP, https://www.ncbi.nlm.nih.gov/gap
Exome Aggregation Consortium (ExAC) Browser, http://exac.broadinstitute.org/
Genome Aggregation Database (gnomAD), http://gnomad.broadinstitute.org/
GME Variome, http://igm.ucsd.edu/gme
GTEx Portal, https://www.gtexportal.org/home/
HomozygosityMapper, http://www.homozygositymapper.org/
OMIM, http://www.omim.org
MutationTaster, http://www.mutationtaster.org/
Python, https://www.python.org
RefSeq, http://www.ncbi.nlm.nih.gov/RefSeq
SimulConsult measurement resources, http://www.simulconsult.com/resources/measurement.html

References

1. Schwarz, D.S., and Blower, M.D. (2016). The endoplasmic reticulum: Structure, function and response to cellular signaling. Cell. Mol. Life Sci. *73*, 79–94.
2. Voeltz, G.K., Rolls, M.M., and Rapoport, T.A. (2002). Structural organization of the endoplasmic reticulum. EMBO Rep. *3*, 944–950.
3. Zhang, H., and Hu, J. (2016). Shaping the endoplasmic reticulum into a social network. Trends Cell Biol. *26*, 934–943.
4. Westrate, L.M., Lee, J.E., Prinz, W.A., and Voeltz, G.K. (2015). Form follows function: The importance of endoplasmic reticulum shape. Annu. Rev. Biochem. *84*, 791–811.
5. Blackstone, C. (2018). Hereditary spastic paraplegia. Handb. Clin. Neurol. *148*, 633–652.
6. Zhao, X., Alvarado, D., Rainier, S., Lemons, R., Hedera, P., Weber, C.H., Tukel, T., Apak, M., Heiman-Patterson, T., Ming, L., et al. (2001). Mutations in a newly identified GTPase gene cause autosomal dominant hereditary spastic paraplegia. Nat. Genet. *29*, 326–331.
7. Züchner, S., Wang, G., Tran-Viet, K.N., Nance, M.A., Gaskell, P.C., Vance, J.M., Ashley-Koch, A.E., and Pericak-Vance, M.A. (2006). Mutations in the novel mitochondrial protein REEP1 cause hereditary spastic paraplegia type 31. Am. J. Hum. Genet. *79*, 365–369.
8. Montenegro, G., Rebelo, A.P., Connell, J., Allison, R., Babalini, C., D'Aloia, M., Montieri, P., Schüle, R., Ishiura, H., Price, J., et al. (2012). Mutations in the ER-shaping protein reticulon 2 cause the axon-degenerative disorder hereditary spastic paraplegia type 12. J. Clin. Invest. *122*, 538–544.
9. Esteves, T., Durr, A., Mundwiller, E., Loureiro, J.L., Boutry, M., Gonzalez, M.A., Gauthier, J., El-Hachimi, K.H., Depienne, C., Muriel, M.P., et al. (2014). Loss of association of REEP2 with membranes leads to hereditary spastic paraplegia. Am. J. Hum. Genet. *94*, 268–277.
10. Chen, S., Novick, P., and Ferro-Novick, S. (2012). ER network formation requires a balance of the dynamin-like GTPase Sey1p and the Lunapark family member Lnp1p. Nat. Cell Biol. *14*, 707–716.
11. Montavon, T., Soshnikova, N., Mascrez, B., Joye, E., Thevenet, L., Splinter, E., de Laat, W., Spitz, F., and Duboule, D. (2011). A regulatory archipelago controls Hox genes transcription in digits. Cell *147*, 1132–1145.
12. Spitz, F., Gonzalez, F., and Duboule, D. (2003). A global control region defines a chromosomal regulatory landscape containing the HoxD cluster. Cell *113*, 405–417.
13. Wang, S., Tukachinsky, H., Romano, F.B., and Rapoport, T.A. (2016). Cooperation of the ER-shaping proteins atlastin, lunapark, and reticulons to generate a tubular membrane network. eLife *5*. https://doi.org/10.7554/eLife.18605.
14. Moriya, K., Nagatoshi, K., Noriyasu, Y., Okamura, T., Takamitsu, E., Suzuki, T., and Utsumi, T. (2013). Protein N-myristoylation plays a critical role in the endoplasmic reticulum morphological change induced by overexpression of protein Lunapark, an integral membrane protein of the endoplasmic reticulum. PLoS ONE *8*, e78235.
15. Chen, S., Desai, T., McNew, J.A., Gerard, P., Novick, P.J., and Ferro-Novick, S. (2015). Lunapark stabilizes nascent three-way junctions in the endoplasmic reticulum. Proc. Natl. Acad. Sci. USA *112*, 418–423.
16. Shemesh, T., Klemm, R.W., Romano, F.B., Wang, S., Vaughan, J., Zhuang, X., Tukachinsky, H., Kozlov, M.M., and Rapoport, T.A. (2014). A model for the generation and interconversion of ER morphologies. Proc. Natl. Acad. Sci. USA *111*, E5243–E5251.
17. Ghila, L., and Gomez, M. (2008). The evolutionarily conserved gene LNP-1 is required for synaptic vesicle trafficking and synaptic transmission. Eur. J. Neurosci. *27*, 621–630.
18. Dixon-Salazar, T.J., Silhavy, J.L., Udpa, N., Schroth, J., Bielas, S., Schaffer, A.E., Olvera, J., Bafna, V., Zaki, M.S., Abdel-Salam, G.H., et al. (2012). Exome sequencing can improve diagnosis and alter patient management. Sci. Transl. Med. *4*, 138ra78.

19. Scott, E.M., Halees, A., Itan, Y., Spencer, E.G., He, Y., Azab, M.A., Gabriel, S.B., Belkadi, A., Boisson, B., Abel, L., et al.; Greater Middle East Variome Consortium (2016). Characterization of Greater Middle Eastern genetic variation for enhanced disease gene discovery. Nat. Genet. *48*, 1071–1076.
20. Lek, M., Karczewski, K.J., Minikel, E.V., Samocha, K.E., Banks, E., Fennell, T., O'Donnell-Luria, A.H., Ware, J.S., Hill, A.J., Cummings, B.B., et al.; Exome Aggregation Consortium (2016). Analysis of protein-coding genetic variation in 60,706 humans. Nature *536*, 285–291.
21. Seelow, D., and Schuelke, M. (2012). HomozygosityMapper2012–Bridging the gap between homozygosity mapping and deep sequencing. Nucleic Acids Res. *40*, W516–W520.
22. Schwarz, J.M., Rödelsperger, C., Schuelke, M., and Seelow, D. (2010). MutationTaster evaluates disease-causing potential of sequence alterations. Nat. Methods *7*, 575–576.
23. Luarte, A., Cornejo, V.H., Bertin, F., Gallardo, J., and Couve, A. (2018). The axonal endoplasmic reticulum: One organelle-many functions in development, maintenance, and plasticity. Dev. Neurobiol. *78*, 181–208.
24. Bozzola, J.J. (1992). Electron microscopy (Wiley Online Library).
25. Harding, H.P., Zeng, H., Zhang, Y., Jungries, R., Chung, P., Plesken, H., Sabatini, D.D., and Ron, D. (2001). Diabetes mellitus and exocrine pancreatic dysfunction in *Perk*$^{-/-}$ mice reveals a role for translational control in secretory cell survival. Mol. Cell *7*, 1153–1163.
26. Howard, V., and Reed, M. (2004). Unbiased stereology: Three-dimensional measurement in microscopy (Garland Science).
27. Zhu, P.P., Soderblom, C., Tao-Cheng, J.H., Stadler, J., and Blackstone, C. (2006). SPG3A protein atlastin-1 is enriched in growth cones and promotes axon elongation during neuronal development. Hum. Mol. Genet. *15*, 1343–1353.
28. Casey, A.K., Chen, S., Novick, P., Ferro-Novick, S., and Wente, S.R. (2015). Nuclear pore complex integrity requires Lnp1, a regulator of cortical endoplasmic reticulum. Mol. Biol. Cell *26*, 2833–2844.
29. Wang, S., Powers, R.E., Gold, V.A., and Rapoport, T.A. (2018). The ER morphology-regulating lunapark protein induces the formation of stacked bilayer discs. Life Sci. Alliance *1*. https://doi.org/10.26508/lsa.201700014.
30. Dürr, A., Camuzat, A., Colin, E., Tallaksen, C., Hannequin, D., Coutinho, P., Fontaine, B., Rossi, A., Gil, R., Rousselle, C., et al. (2004). Atlastin1 mutations are frequent in young-onset autosomal dominant spastic paraplegia. Arch. Neurol. *61*, 1867–1872.
31. Orlacchio, A., Montieri, P., Babalini, C., Gaudiello, F., Bernardi, G., and Kawarai, T. (2011). Late-onset hereditary spastic paraplegia with thin corpus callosum caused by a new SPG3A mutation. J. Neurol. *258*, 1361–1363.
32. Wheway, G., Schmidts, M., Mans, D.A., Szymanska, K., Nguyen, T.T., Racher, H., Phelps, I.G., Toedt, G., Kennedy, J., Wunderlich, K.A., et al.; UK10K Consortium; and University of Washington Center for Mendelian Genomics (2015). An siRNA-based functional genomics screen for the identification of regulators of ciliogenesis and ciliopathy genes. Nat. Cell Biol. *17*, 1074–1087.
33. Roosing, S., Hofree, M., Kim, S., Scott, E., Copeland, B., Romani, M., Silhavy, J.L., Rosti, R.O., Schroth, J., Mazza, T., et al. (2015). Functional genome-wide siRNA screen identifies KIAA0586 as mutated in Joubert syndrome. eLife *4*, e06602.

The American Journal of Human Genetics, Volume *103*

Supplemental Data

Mutations in *LNPK*, Encoding the Endoplasmic Reticulum Junction Stabilizer Lunapark, Cause a Recessive Neurodevelopmental Syndrome

Martin W. Breuss, An Nguyen, Qiong Song, Thai Nguyen, Valentina Stanley, Kiely N. James, Damir Musaev, Guoliang Chai, Sara A. Wirth, Paula Anzenberg, Renee D. George, Anide Johansen, Shaila Ali, Muhammad Zia-ur-Rehman, Tipu Sultan, Maha S. Zaki, and Joseph G. Gleeson

Supplemental Figures and Tables

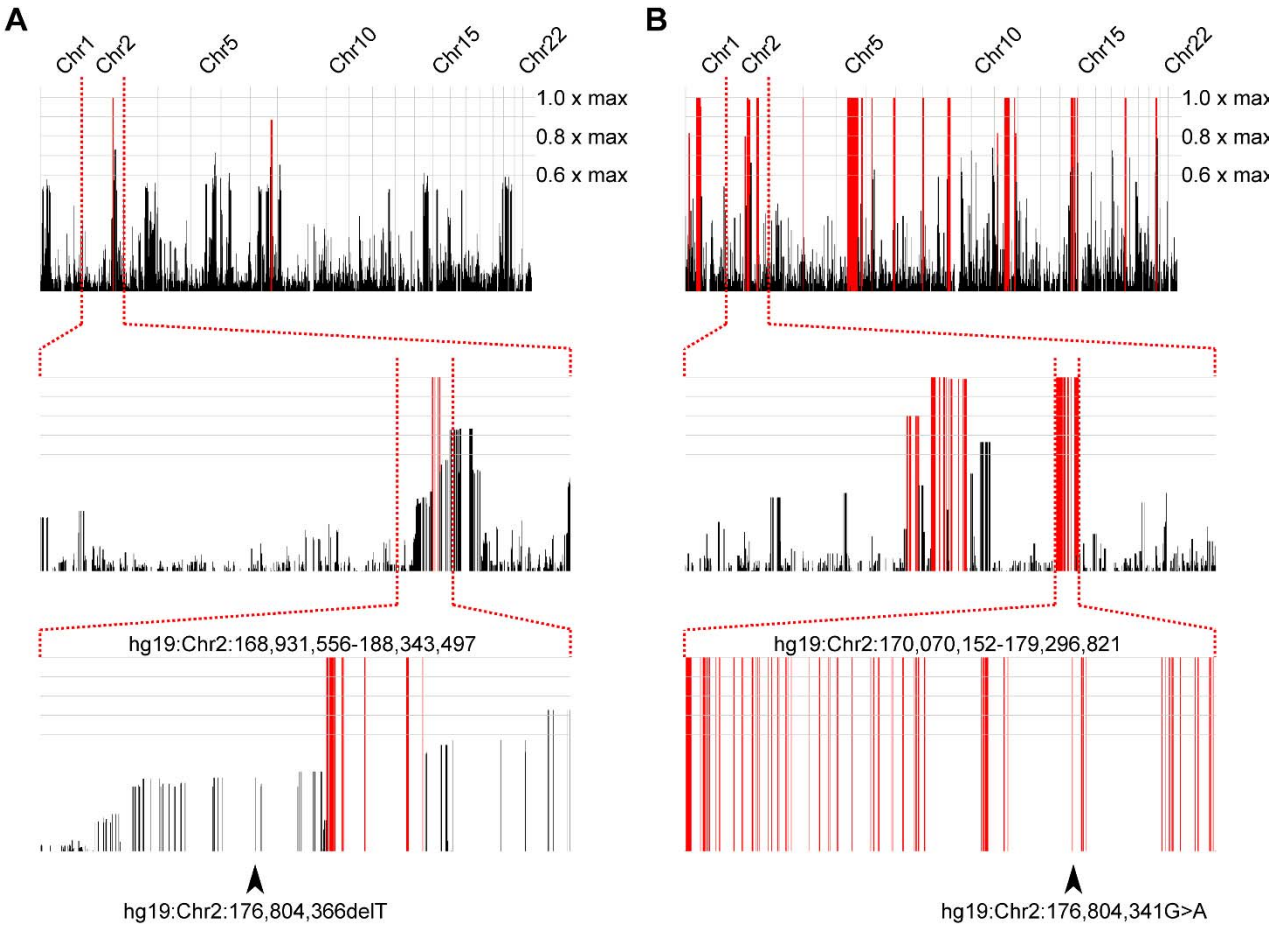

Figure S1. Homozygosity plots for families A and B.

(A-B) Graphical representation of the homzygosity plots generated by HomozygosityMapper for all 22 autosomes for the affected individuals in Family A (A) and B (B). Red peaks indicate homozygosity scores above the cutoff at 0.8x of the maximum. There is an extensive stretch of homozygosity on chromosome 2. Arrowheads in the lowest panel indicate the positions of the mutations. While the mutation in Family A lies just outside the significant stretch of homozygosity, manual inspection of the area revealed that sites contributing negatively to the score were generally of low quality, suggesting that the mutation most likely lies within this stretch of extended homozygosity.

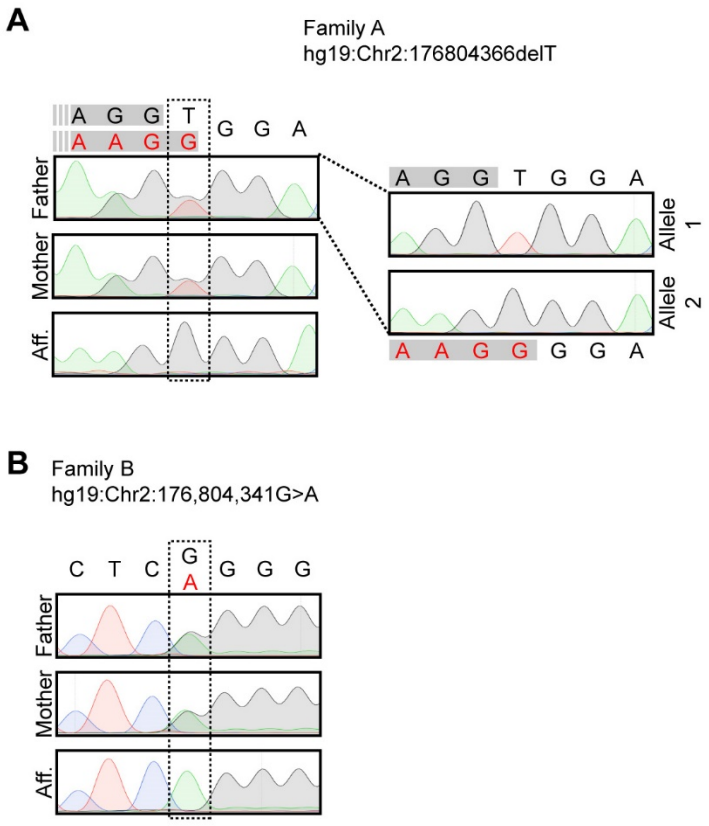

Figure S2. Sanger sequencing traces for families A and B.

(A) Sanger sequencing traces depicting the T deletion present in Family A that results in the frameshift mutation. For better clarity the two heterozygous alleles from the father are shown separated as well. Shown are traces for father, mother, and one of the two affected boys (Aff.); as expected from WES analysis, both parents are heterozygous and the affected child is homozygous for the mutation.

(B) Sanger sequencing traces depicting the G>A conversion present in Family B that results in the premature stop codon. Shown are traces for father, mother, and the affected girl (Aff.); as expected from WES analysis, both parents are heterozygous and the affected child is homozygous for the mutation.

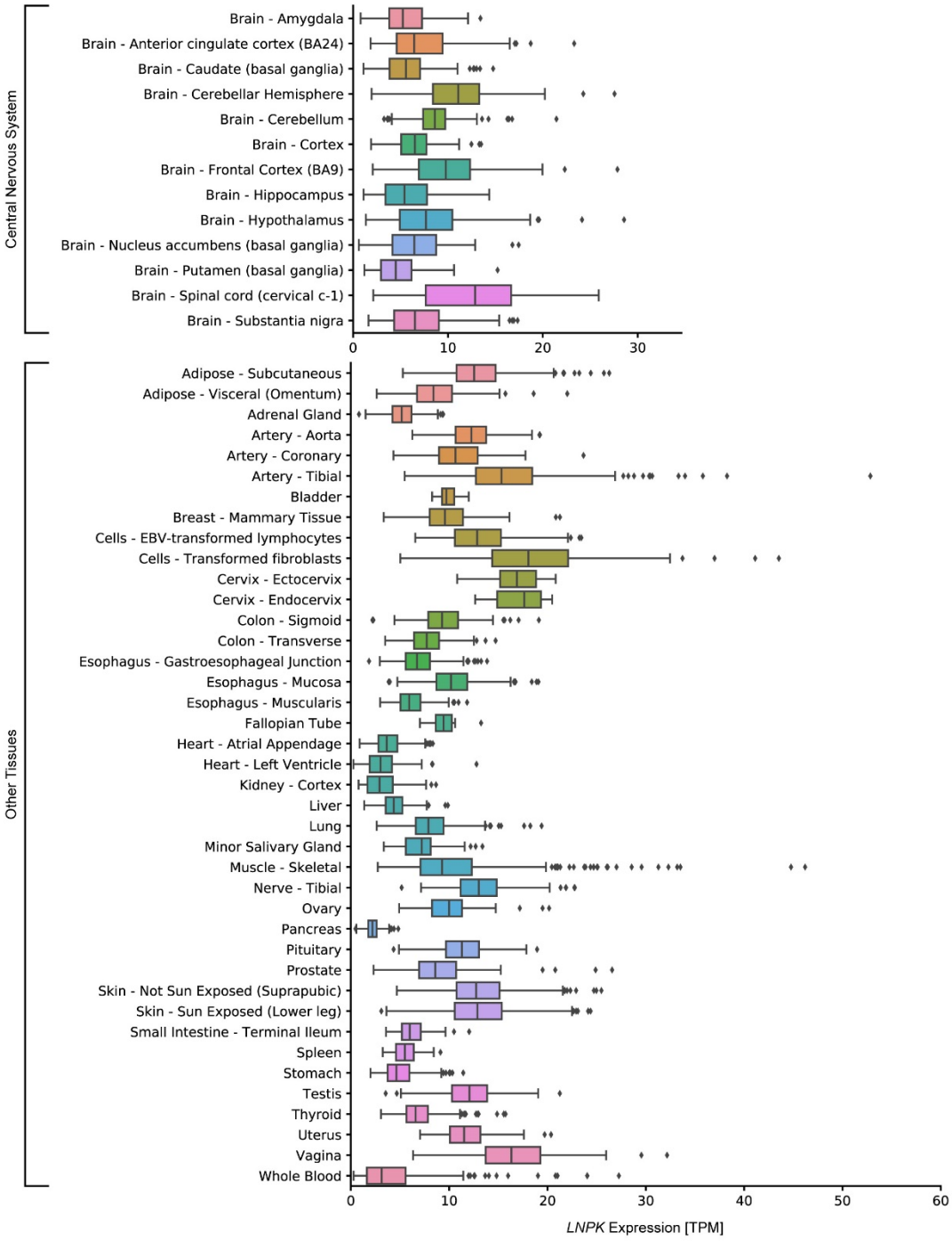

Figure S3. *LNPK* expression across various tissues in adult humans (GTEx data).

Expression analysis of *LNPK* transcripts across various adult tissues. Data is split into expression in the central nervous tissue and other tissues. *LNPK* shows ubiquitous expression

across all tissues. Expression is shown as Transcripts per Kilobase Million (TPM). Data used was derived from the GTEx portal.[33; 34] Shown are standard boxplots with outliers.

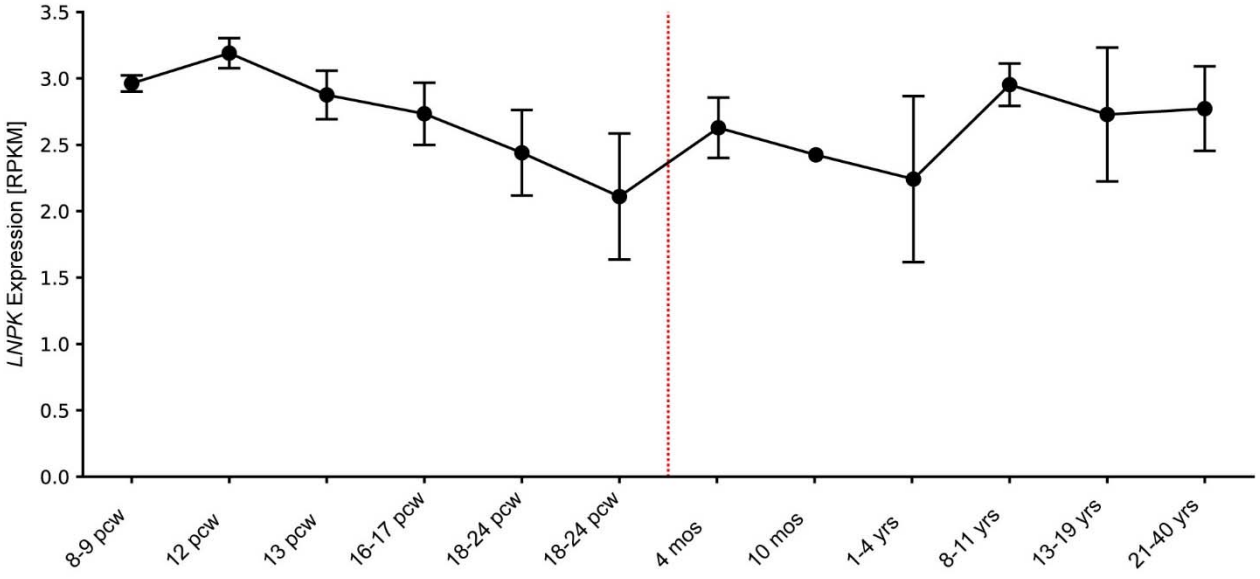

Figure S4. *LNPK* expression in the human cortical region along the developmental trajectory (BrainSpan data).

Expression analysis of *LNPK* transcripts in the developing and adult cortical regions. *LNPK* shows ubiquitous expression across all time points. Expression is shown as Reads Per Kilobase of transcript, per Million mapped reads (RPKM). Data used was derived from RNA-Sequencing data from BrainSpan.[35] Shown are mean ± SD for each time point. pcw: post-conception weeks; mos: months; yrs: years. The red line separates prenatal and postnatal time points.

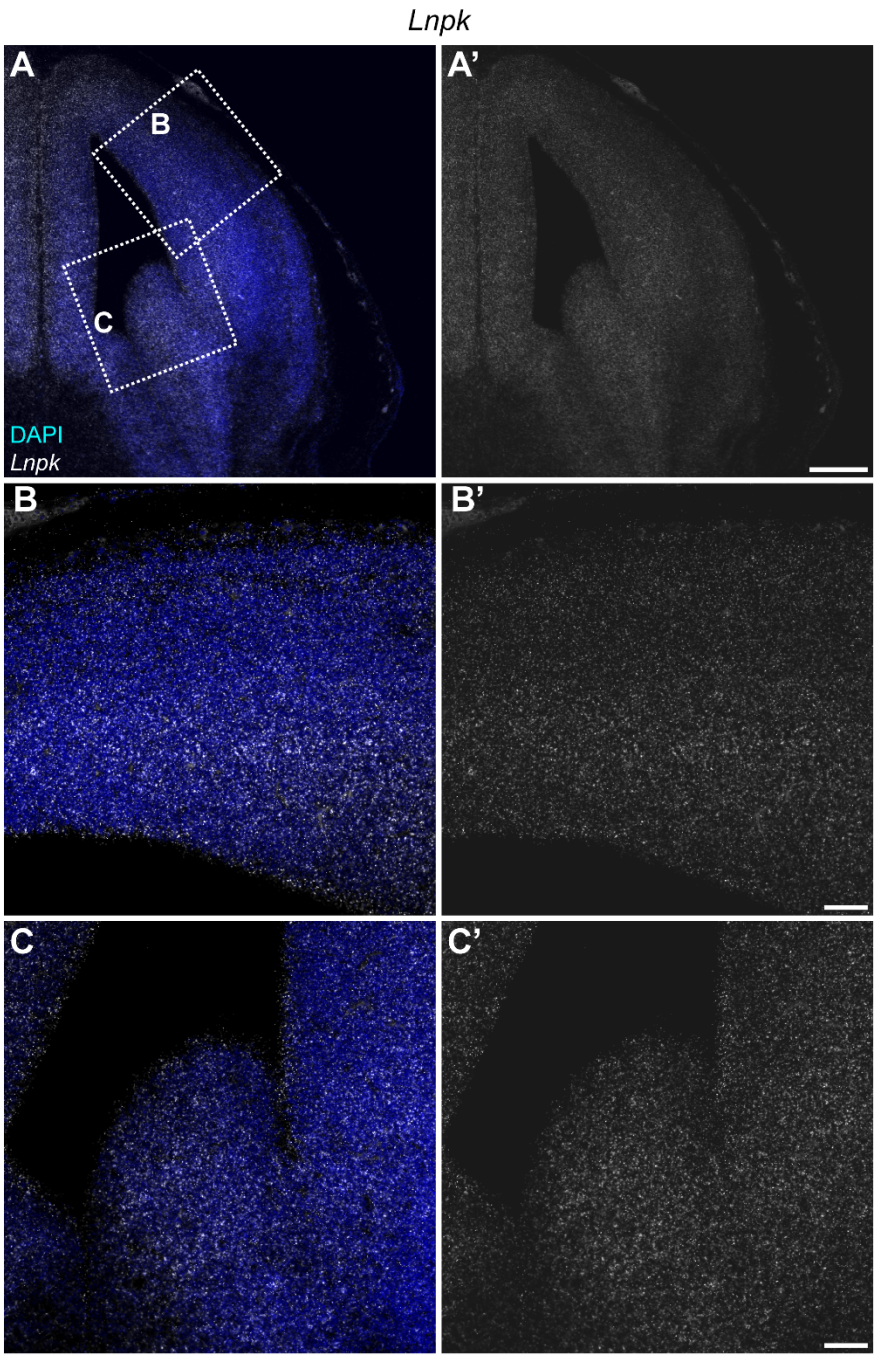

Figure S5. *Lnpk in situ* hybridization using RNAscope.

(A-C) Images of an *in situ* hybridization using RNAscope against the *Lnpk* mRNA transcript. Shown are DAPI and the *in situ* signal. A', B', and C' show *Lnpk* channel in grey scale. B and C are magnified images of the boxed regions in A for the dorsal and ventral cortex, respectively.

Note that Figure 2B was derived from the image shown in B here. *Lnpk* shows ubiquitous expression across the entire developing forebrain. Scale bars show 200 μm in A', and 50 μm in B' and C'.

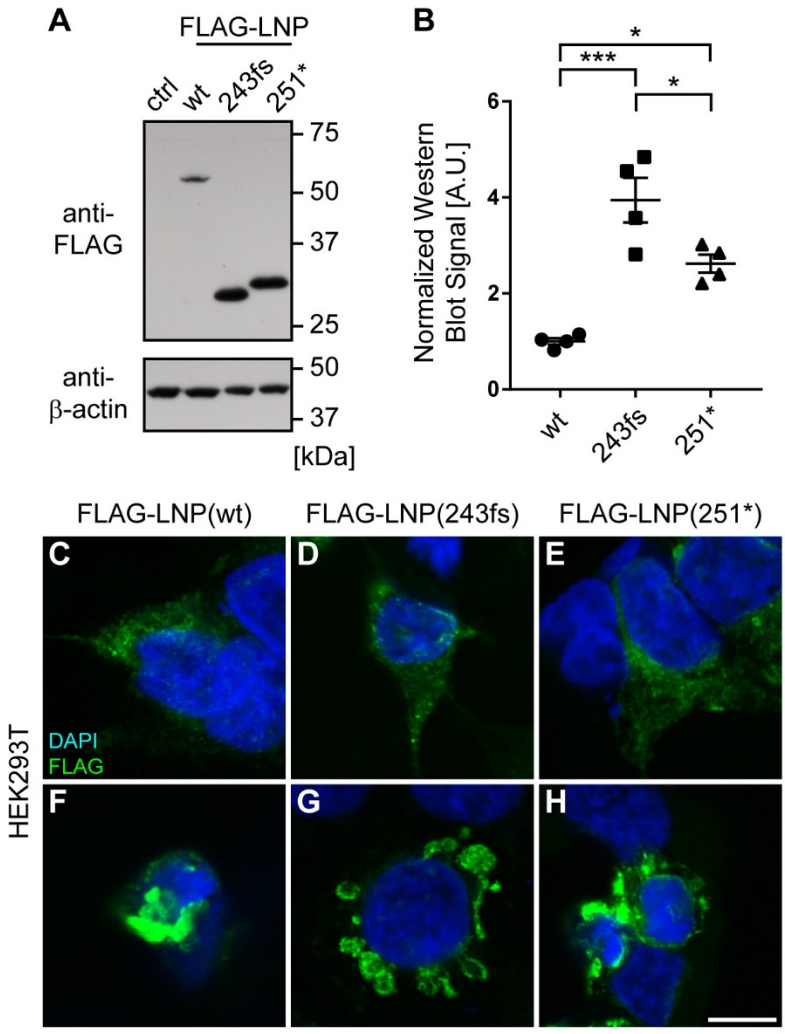

Figure S6. Truncated proteins are stable and appear to maintain correct subcellular localization when overexpressed.

(A) Western blot images probing for the FLAG-tag and β-actin in parallel blots using the same input. Shown is one example of a blot for HEK293T cell lysates following transfection with either no vector (ctrl), or a FLAG-tagged version of wild-type or mutant LNP. The two truncating mutations are abbreviated with 243fs and 251*, respectively.

(B) Quantification of the samples shown in A. FLAG signal was normalized to β-actin. Note that both truncated proteins appear to be more abundant in an overexpression situation, suggesting increased protein stability upon removal of the C-terminal domain. Shown are individual data

points, as well as the mean ± SEM. One-way ANOVA, Tukey multiple comparisons test: *P<0.05, ***P<0.001. n=3 independent experiments.

(C-E) Images for HEK293T cells overexpressing FLAG-tagged versions of wild-type or mutant LNP at moderate levels. Cells are stained with DAPI and an antibody recognizing the FLAG-tag. Subcellular localization of truncated protein resembles that of the wild-type.

(F-H) Images for HEK293T cells overexpressing FLAG-tagged versions of wild-type or mutant LNP at high levels. All variants accumulate in large vesicle-like structures that are distinct from the localization in cell expressing the constructs at moderate levels. Nevertheless, expression patterns are similar between wild-type and mutants. Scale bar shows 10 μm in H.

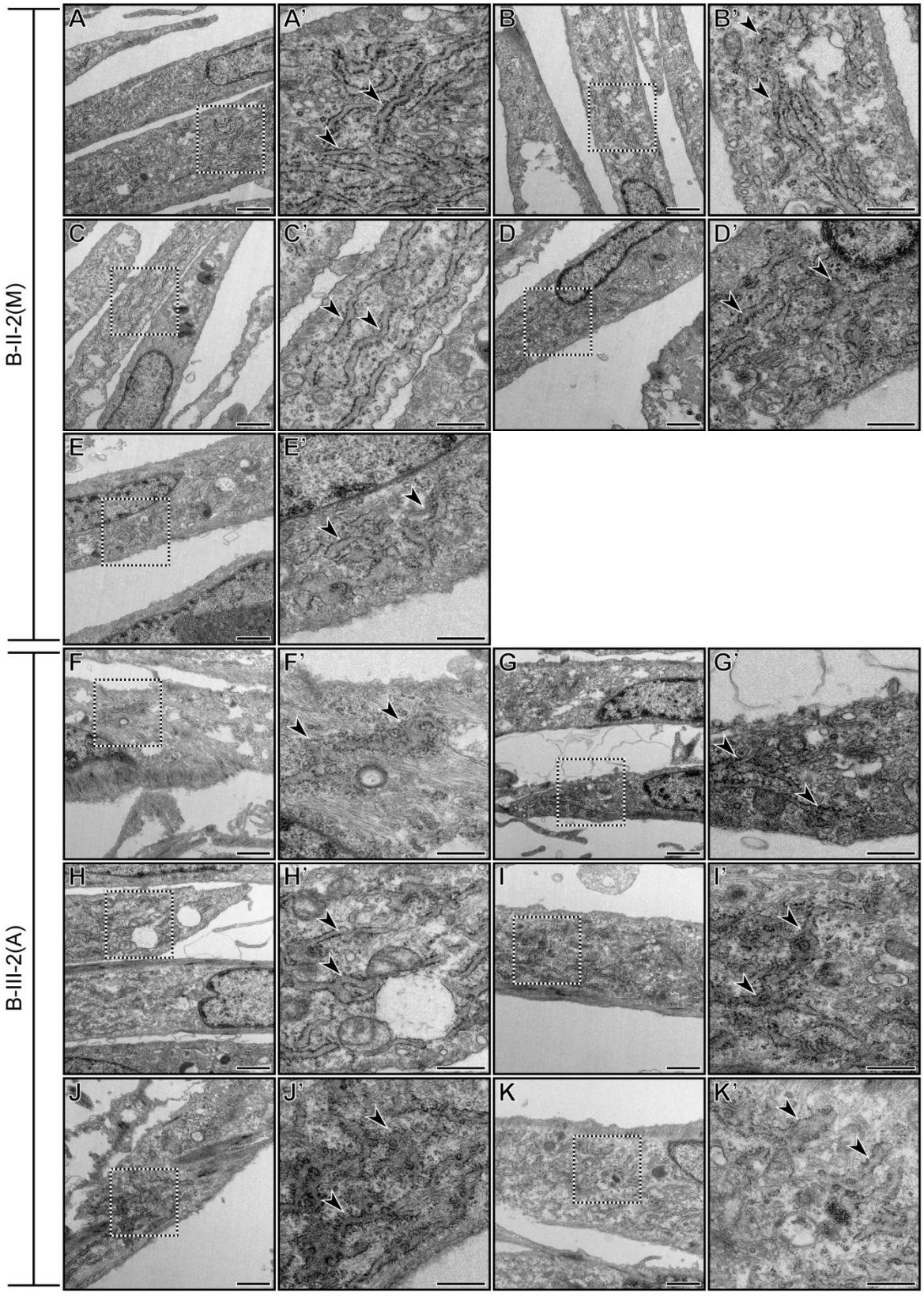
B-II-2(M)
B-III-2(A)
A
A'
B
B''
C
C'
D
D'
E
E'
F
F'
G
G'
H
H'
I
I'
J
J'
K
K'

Figure S7. Fibroblasts with a truncating mutation in *LNPK* show aberrant ER morphology.

(A-K) Series of example images for B-II-2(M) (A-E) and B-III-2(A) (F-K) fibroblasts to illustrate the aberrant ER morphology that is frequently observed in the cells derived from the affected girl. Images marked with ‘ are magnifications of the boxed region in the corresponding image. Arrowheads indicate structures identified as rough ER. Scale bars show 1 μm in A-K, and 500 nm in A’-K’.

Table S1. Mutations in *LNPK* cause various phenotypes, including corpus callosum hypoplasia, hypotonia, and epilepsy – extended clinical table.

ND: no data. SD: standard deviations (calculated using SimulConsult's measurement resources). HC: head circumference. VEP/ERG: visual evoked potential/electroretinography. EMG: electromyography. TMS: tandem mass spectrometry screening for metabolic disease.

Individual	A-III-1	A-III-2	B-III-2
Mutation (genomic)	hg19:Chr2:176804365GT>G	hg19:Chr2:176804365GT>G	hg19:Chr2:176804341G>A
Mutation (protein)	p.Pro243LeufsTer2	p.Pro243LeufsTer2	p.Arg251Ter
Mutation (cDNA)	c.726delA	c.726delA	c.751C>T
Gender	M	M	F
Origin	Egypt	Egypt	Pakistan
Consanguinity	First cousins	First cousins	First cousins
Age at diagnosis	15 y	7 y 4 mos	14 months
Weight at birth (kg)	3 kg (-0.9 SD)	2.8 (-1.2)	2.9 (-1.0)
Length at birth (cm)	51.5 cm (+0.5 SD)	50 (mean)	51 (+0.6)
HC at birth (cm)	33 cm (-1.3 SD)	34 (-0.8)	34 (-0.5)
Weight at last examination (kg), age	58 kg (16 y) (-0.2 SD)	21 (8 y 2 mos) (-1.6)	28kg (13.5 y) (-2.8)
Length at last examination (cm), age	157 cm (16 y) (-1.8 SD)	114 (8 y 2 mos) (-2.5)	139 (13.5 y) (-2.8)

HC at last examination (cm), age	53.5 cm (16 y) (-1.1 SD)	51cm (8 y 2 mos) (-1.0)	52 (13.5 y) (-1.4)
Psychomotor development			
Gross motor	Delayed	Delayed	Significant delay
Fine motor	Delayed	Delayed	Significant delay
Language	Absent	Delayed	Significant delay
Social	Delayed	Delayed	Significant delay
Regression	Progressive	Stationary	Progressive (bedridden)
Neurological findings			
Higher cognitive functions	Severe intellectual disability, no speech, autistic features, very limited social interaction, hyperactivity, inattention, dementia	Intellectual disability, few unclear words, mild autistic features, hyperactive, inattention, minimal aggressiveness	Vegetative state
Extrapyramidal symptoms	Rigidity, drooling	ND	Rigidity
Brainstem findings	No	No	No
Cerebellar deficits	No	No	Bedridden
Vision	Normal	Normal	Normal
Motor deficits	Hypertonia, only crawling	Ambulatory	Flaccid
Muscle tone	Hypotonia with rigidity	Mild hypotonia	Flaccid
Reflexes	Present	Present	Flaccid
Sensory	Normal	Normal	Not possible

Gait	Incapable	Wide based	Ataxia
Seizures			
Onset	2 y	2 y	1 y
Type(s)	Myoclonic, tonic and extension spasm	Myoclonic	Generalized tonic clonic
Most frequent type	Myoclonic	Myoclonic	Generalized tonic clonic
Frequency	Every several days	Controlled	Unknown
Treatment	Valproate, Levetiracetum, Clonazepam	Valproate, Levetiracetum	Valporate, Carbamazepine
Other systemic findings			
Immunodeficiency	No	No	Frequent infections
Musculoskeletal	Feet deviation inward	No	Scoliosis present
Skin	Normal	Hypopigmentation in groin	Normal
MRI findings			
Cerebral cortex	Normal	Normal	Normal
Corpus callosum	Hypoplasia	Hypoplasia	Hypoplasia
Brain stem	Normal	Normal	Normal
Cerebellum	Normal	Mild vermian hypoplasia	Atrophy
Other observations			
Creatine phosphokinase level	Normal	Normal	Normal
Metabolic work up	Normal	Normal	Normal

VEP/ERG	Normal	Normal	Not available
EMG	Normal	Normal	Normal
TMS	Normal	Normal	Normal
Eye	Pigmentation in sclera	Pigmentation in sclera	Normal

Table S2. Primer Sequences.

LNPK_SeqF	CACACACACACACATCCTGT
LNPK_SeqR	ATGGCCTGAAGTGGAAGTCC
LNP_F_FLAGcloning	gggGAATTCATGgactacaaggacgatgacgataagATGGGTGGATTATTTTCTCGAT
LNP_R_FLAGcloning	gggCTCGAGctaCTCTGCCGTCAAAGATTCTC
LNP_243fs_F_mut	ATAGGTCTTGCTAAAGGGGACCTGGAGGATGAAG
LNP_243fs_R_mut	CTTCATCCTCCAGGTCCCCTTTAGCAAGACCTAT
LNP_251*_F_mut	CAAAGCACCTCGTTCTCAGGGGAGAATAGGTCTTG
LNP_251*_R_mut	CAAGACCTATTCTCCCCTGAGAACGAGGTGCTTTG
mmLnpk_qPCR_F	AAGCCAGCTCATTGAAGAC
mmLnpk_qPCR_F	TGTCATCTCTCTGCTCAGTAC
hsLNPK_qPCR_F	GTCATCTGTCTGCTCTGTATTATC
hsLNPK_qPCR_R	TGCTTTCATCAGACAACCAG
mmPgk1_qPCR_F	AAAGTCAGCCATGTGAGCACT
mmPgk1_qPCR_R	ACTTAGGAGCACAGGAACCAAA
mmTfrc_qPCR_2F	TCGCTTATATTGGGCAGACC
mmTfrc_qPCR_2R	ATCCAGCCTCACGAGGAGT
mmHprt_qPCR_3F	GAACCAGGTTATGACCTAGATTTGTT
mmHprt_qPCR_3R	CAAGTCTTTCAGTCCTGTCCATAAT
hsHPRT_qPCR_F	TGACACTGGCAAAACAATGCA
hsHPRT_qPCR_R	GGTCCTTTTCACCAGCAAGCT
hsPGK1_qPCR_F	ATGGATGAGGTGGTGAAAGC
hsPGK1_qPCR_R	CAGTGCTCACATGGCTGACT
hsTBP_qPCR_F	TGCACAGGAGCCAAGAGTGAA
hsTBP_qPCR_R	CACATCACAGCTCCCCACCA

Supplemental Materials and Methods

Recruitment. The procedures followed for recruitment and data collection were in accordance with the ethical standards of the responsible committee on human experimentation at the respective, participating institute and proper informed consent was obtained.

DNA extraction and whole exome sequencing. DNA was extracted on an Autopure LS instrument (Qiagen, Valencia, CA) with Autopure chemistry according to the manufacturer's instructions. Samples of the three affected individuals and the two unaffected parents were subjected to Agilent Sure-Select Human All Exon v2.0 (44Mb baited target) library preparation sequencing on an Illumina HiSeq 2000 with v2 chemistry (Read Length: 151). The accession number for these data is dbGAP: phs000288.v1.p1.

Computational analysis. Variant calling and filtering were performed according to our previously described whole exome sequencing pipeline.[1] Variants were filtered if not present in both affected in Family A. For both families, they were filtered if the minor allele frequency (MAF) was >1:10,000, or if they yielded PolyPhen-2 prediction scores of <0.9 or GERP score <4.5. Calls were also checked with MutationTaster and homozygosity was confirmed using the online tool HomozygosityMapper.[2-4]

Sanger sequencing. Sanger sequencing of PCR products covering exon 10 of *LNPK* was performed using standard procedures (LNPK_SeqF/R; Table S2). Individual allele sequences were obtained by TOPO TA cloning (Life Technologies, 450641) and colony PCR according to the manufacturer's instructions and standard protocols. Sequencing tracks were visualized with SnapGene Viewer (SnapGene).

Cell culture experiments and immunocytochemistry. Cell culture maintenance and transfection was described previously.[5] Fibroblasts (obtained from dermal biopsies and ATCC for the control) and NPCs were generated and cultured as described before.[6] N-terminally FLAG-tagged LNP was cloned using the sequence in the Lnp1-GFP vector, a kind gift of the Ferro-Novick laboratory, into the pcDNA3.1+ vector (LNP_F/R_FLAGcloning; Table S2).[7] The mutations were introduced using the Quikchange Lightning Site-Directed Mutagenesis Kit according to the manufacturer's instructions (Agilent Technologies, 210518; LNP_243fs/251*_F/R_Q5Mut; Table S2). Constructs were transfected the day before fixation and staining. Transfected cells, fibroblasts, and NPCs were fixed in 4% paraformaldehyde and immunocytochemistry was performed using standard protocols. The employed antibodies were: anti-DDDDK tag (Abcam, ab1162, 1:1000), anti-Lunapark (Sigma-Aldrich, HPA014205, 1:200), anti-SOX2 (Santa Cruz, sc-17320, 1:200), and anti-TUBB3 (Tuj1, BioLegend, 801202, 1:1000). Cells were counterstained with DAPI (Thermo Fisher, D1306, 1:2000). Images were acquired with a Leica SP5 microscope and processed with ImageJ/Fiji.[8; 9]

Quantitative RT-PCR. RNA extraction, cDNA synthesis, and qPCR were performed as described previously.[10] Primers employed are listed in Table S2.

RNAscope in situ *hybridization*. *In situ* hybridization was performed using RNAscope technology (Advanced Cell Diagnostics, 322000) with custom probes against *Lnpk* (Advanced Cell Diagnostics).[11] Images were acquired with a Leica SP5 microscope and processed with ImageJ/Fiji.

Western blot. Cells were lysed with ice-cold RIPA buffer and assessed by Western blot using standard protocols. Primary antibodies used were anti-beta-Actin (Santa Cruz, sc-47778, 1:2000), anti-FLAG-tag (Sigma, F3165, 1:1000), and anti-Lunapark (Sigma-Aldrich,

HPA014205, 1:1000). Western blot signal intensity (area of peaks) was analyzed using ImageJ/Fiji and normalized to the loading control.

Transmission electron microscopy and analysis. Fibroblasts were immersed in modified Karnovsky's fixative (2% glutaraldehyde in 0.1M sodium cacodylate buffer, pH 7.4) for 30 minutes at room temperature, scraped and pelleted and resuspended in fresh fixative again for at least 4 hours at 4°C, postfixed in 1% osmium tetroxide in 0.1M cacodylate buffer for 1 hour and stained *en bloc* in 2% uranyl acetate for 1 hour. Pellets were dehydrated in ethanol, embedded in Durcupan epoxy resin (Sigma-Aldrich), sectioned at 50 to 60 nm on a Leica UCT ultramicrotome, and picked up on 300 mesh copper grids. Sections were stained with 2% uranyl acetate for 5 minutes and Sato's lead stain for 1 minute. Grids were viewed using a JEOL 1200EX II (JEOL, Peabody, MA) transmission electron microscope and photographed using a Gatan digital camera (Gatan, Pleasanton, CA). EM images were automatically anonymized and analyzed by a person blind to the conditions and the expected phenotypes. Unbiased stereology was achieved using ImageJ/Fiji by overlaying a grid with an area of 100000 pixels^2 per point on images with an image as shown in Figure 4B (4090x4090 pixels).[12] Each grid point was assessed in order to determine whether it was overlaying an intact cell, and whether it was overlaying rough ER or not. The coordinates were then imported using Python (3.64) (Python Software Foundation, https://www.python.org/) with Pandas (0.22.0).[13] These data were then directly used for the analysis of fractional abundance ([points within rough ER]/[all points within cellular area]). For grey value analysis, images were imported as NumPy (1.13.3) matrices using Scikit-image (0.13.0).[14; 15] In order to reduce variability due to single pixel measurements, average grey values were obtained by averaging the grey values of a square of 5x5 pixels, centered around the coordinates of each point. In addition all values were normalized for the varying background intensities; these were obtained by measuring 5 points representing

background intensities from the four corners and the middle of the image (as much spaced apart as possible) and using squares of 21x21pixels.

GTEx and BrainSpan. Data was obtained from the GTEx and BrainSpan (© 2010 BrainSpan Atlas of the Developing Human Brain. Available from brainspan.org) portals and processed using Python (3.64) with Pandas (0.22.0).

Visualization and statistical analysis. Statistical analysis was done as indicated in figure legends using GraphPad Prism 7. Visualization of data was performed using GraphPad Prism 7 (Figures 2, 3, and S6) or using Python (3.64) with Seaborn (0.8.1).[16]

Supplementary References

1. Dixon-Salazar, T.J., Silhavy, J.L., Udpa, N., Schroth, J., Bielas, S., Schaffer, A.E., Olvera, J., Bafna, V., Zaki, M.S., Abdel-Salam, G.H., et al. (2012). Exome sequencing can improve diagnosis and alter patient management. Sci Transl Med 4, 138ra178.
2. Seelow, D., and Schuelke, M. (2012). HomozygosityMapper2012--bridging the gap between homozygosity mapping and deep sequencing. Nucleic Acids Res 40, W516-520.
3. Seelow, D., Schuelke, M., Hildebrandt, F., and Nurnberg, P. (2009). HomozygosityMapper--an interactive approach to homozygosity mapping. Nucleic Acids Res 37, W593-599.
4. Schwarz, J.M., Rodelsperger, C., Schuelke, M., and Seelow, D. (2010). MutationTaster evaluates disease-causing potential of sequence alterations. Nat Methods 7, 575-576.
5. Breuss, M.W., Nguyen, T., Srivatsan, A., Leca, I., Tian, G., Fritz, T., Hansen, A.H., Musaev, D., McEvoy-Venneri, J., James, K.N., et al. (2017). Uner Tan syndrome caused by a homozygous TUBB2B mutation affecting microtubule stability. Hum Mol Genet 26, 258-269.
6. Akizu, N., Cantagrel, V., Schroth, J., Cai, N., Vaux, K., McCloskey, D., Naviaux, R.K., Van Vleet, J., Fenstermaker, A.G., Silhavy, J.L., et al. (2013). AMPD2 regulates GTP synthesis and is mutated in a potentially treatable neurodegenerative brainstem disorder. Cell 154, 505-517.
7. Chen, S., Desai, T., McNew, J.A., Gerard, P., Novick, P.J., and Ferro-Novick, S. (2015). Lunapark stabilizes nascent three-way junctions in the endoplasmic reticulum. Proc Natl Acad Sci 112, 418-423.
8. Rueden, C.T., Schindelin, J., Hiner, M.C., DeZonia, B.E., Walter, A.E., Arena, E.T., and Eliceiri, K.W. (2017). ImageJ2: ImageJ for the next generation of scientific image data. BMC Bioinformatics 18, 529.
9. Schindelin, J., Arganda-Carreras, I., Frise, E., Kaynig, V., Longair, M., Pietzsch, T., Preibisch, S., Rueden, C., Saalfeld, S., Schmid, B., et al. (2012). Fiji: an open-source platform for biological-image analysis. Nat Methods 9, 676-682.
10. Breuss, M., Heng, J., Poirier, K., Tian, G., Jaglin, X., Qu, Z., Braun, A., Gstrein, T., Ngo, L., Haas, M., et al. (2012). Mutations in the β-Tubulin Gene TUBB5 Cause Microcephaly with Structural Brain Abnormalities. Cell Rep 2, 1554-1562.
11. Feng, J., Xian, Q., Guan, T., Hu, J., Wang, M., Huang, Y., So, K.F., Evans, S.M., Chai, G., Goffinet, A.M., et al. (2016). Celsr3 and Fzd3 Organize a Pioneer Neuron Scaffold to Steer Growing Thalamocortical Axons. Cereb Cortex 26, 3323-3334.
12. Howard, V., and Reed, M. (2004). Unbiased stereology: three-dimensional measurement in microscopy.(Garland Science).
13. McKinney, W. (2010). Data Structures for Statistical Computing in Python. In Proceedings of the 9th Python in Science Conference, S.v.d. Walt and J. Millman, eds., pp 51-56.
14. Oliphant, T.E. (2006). A guide to NumPy.(Trelgol Publishing USA).
15. van der Walt, S., Schonberger, J.L., Nunez-Iglesias, J., Boulogne, F., Warner, J.D., Yager, N., Gouillart, E., Yu, T., and scikit-image, c. (2014). scikit-image: image processing in Python. PeerJ 2, e453.
16. Waskom, M., Botvinnik, O., O?Kane, D., Hobson, P., Lukauskas, S., Gemperline, D.C., Augspurger, T., Halchenko, Y., Cole, J.B., Warmenhoven, J., et al. (2017). mwaskom/seaborn: v0.8.1 (September 2017). In. (